Operational Regions of a Multi-Kite AWE System

Rachel Leuthold[1], Jochem De Schutter[1], Elena C. Malz[2], Giovanni Licitra[3], Sébastien Gros[2], and Moritz Diehl[1]

Abstract— **Multiple-kite airborne wind energy systems (MAWES) aim to efficiently harvest the stronger, less-intermittent winds at high altitude without material-intensive towers. Solving a series of optimal control problems for two-kite MAWES, we show that pumping-cycle MAWES have three distinct operational regions: Region I, where power is consumed to stay aloft; Region II, where the power harvesting factor grows until the design wind speed; and Region III, where the power extraction is curtailed so as to respect the physical limitations of the system. The actuator disk (AD) method is arguably the simplest tool to model aerodynamic induction effects, though its validity is limited. In this paper, we show that AD is not valid for Region I.**

I. INTRODUCTION

Airborne wind energy (AWE) systems harvest the stronger, less-intermittent winds at high altitude without material-intensive towers. In AWE systems, kites fly crosswind to produce power either in a pumping-cycle, using a ground-station generator turned as the tether reels in and out, or in drag-mode, using an on-board turbine [1]. Multiple-kite airborne wind energy systems (MAWES) are an AWE system concept where orbiting kites balance the forces on the main tether in order to increase system efficiency.

Launching may be the most expensive portion of MAWES operation. As such, MAWES economic viability depends heavily on the model used to decide whether to remain aloft or to land and re-launch. The system should only land when re-launching is less expensive than continued flight considering, for example, fatigue damage in strong winds and energy expenditure in low winds. To ensure the validity of the landing-decision modelling assumptions, there must be a rough idea of MAWES behavior over a range of wind velocities.

However, the existing literature does not yet show the relationship between wind velocity and system behavior for pumping-cycle MAWES with simplified wake modelling and six degree of freedom kite dynamics. This existing literature describes: the behavior of point-mass kites in pumping-cycle [2]; the relative advantages of drag-mode MAWES over single-kite systems [3]; model predictive control strategies for drag-mode MAWES [4]; the impact of actuator disk

(AD) modelling on drag-mode power output [5]; and AD modelling of rotationally-steady reel-out behaviors [6].

In this paper, a series of optimal control problems (OCP) are solved for a two-kite MAWES, to consider two questions. First, can MAWES behavior be grouped into distinct operational regions by wind speed? Second, does the resulting MAWES behavior indicate preliminary restrictions to model selection? Section II describes a simplified MAWES model; Section III, the OCP to be solved; Section IV, some results; with conclusions given in Section V.

II. SIMPLIFIED MAWES MODEL

The model of the MAWES incorporates the aerodynamic forces and moments acting on the system components into an expressions of the system dynamics.

A. Geometry

The MAWES is placed in an earth-fixed coordinate frame, whose origin is where the main tether joins the winch. Then, $\hat{\boldsymbol{x}}$ points in the dominant wind direction; $\hat{\boldsymbol{y}}$, across the wind window, and $\hat{\boldsymbol{z}}$, vertically upwards.
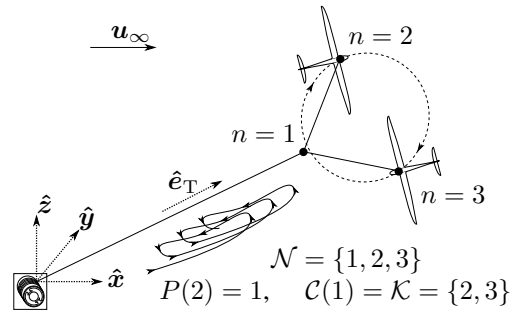

Fig. 1: MAWES geometry, as described by tree structure

The MAWES geometry is represented as a tree structure, shown in Figure 1 and described in more detail in [3], with nodes $n \in \mathcal{N}$ that demarcate the top of every tether segment. Some of these nodes are 'kite' nodes $k \in \mathcal{K} \subset \mathcal{N}$. In this tree structure, each node has a 'parent' named $P(n)$. The set of nodes with parent n is named $\mathcal{C}(n)$.

Every node n has states that describe the position $\boldsymbol{q}_n$ and velocity $\dot{\boldsymbol{q}}_n$ of the top of its tether segment. The tether segments are straight, homogeneous, and cannot carry compressive forces. Note that this analysis assumes an undiscretized main tether with diameter $d_T = d_1$ and length $l_T = l_1$ and orientation $\hat{\boldsymbol{e}}_T = \boldsymbol{q}_1 / \|\boldsymbol{q}_1\|_2$, as well as secondary tethers with diameters $d_S = d_n$ and lengths $l_S = l_n$, for $n > 1$.

[1] Rachel Leuthold, Jochem De Schutter and Moritz Diehl are with the Dept. of Microsystems Engineering, University of Freiburg, 79110 Freiburg, Germany (rachel.colette.leuthold@imtek.uni-freiburg.de)
[2] Elena C. Malz and Sébastien Gros are with the Dept. of Electrical Engineering, Chalmers University, 41258 Göteborg, Sweden
[3] Giovanni Licitra is with the Dept. of Microsystems Engineering, University of Freiburg, 79110 Freiburg, Germany, and Ampyx Power, 2521 AL Den Haag, Netherlands

TABLE I: MAWES modelling parameters

sym.	value	src.	sym.	value	src.
b	5.5 m	[8]	ρ_{d}	970 kg/m^3	[9]
c_{ref}	0.55 m	[8]	f_{s}	10	
m_{K}	36.8 kg	[8]	$\sigma_{\max}$	3.6 GPa	[9]
$\boldsymbol{J}_{xx}$	25 kg m^2	[8]	C_{T}	1.0	[10]
$\boldsymbol{J}_{yy}$	32 kg m^2	[8]	z_{ref}	10 m	[11]
$\boldsymbol{J}_{zz}$	56 kg m^2	[8]	z_0	0.1 m	[11]
$\boldsymbol{J}_{xz}$	0.47 kg m^2	[8]	γ	1.4	[10]
m_{W}	100 kg		R	287 J/kg/K	[10]
$C_{\mathrm{L},0}$	0.528	[12]	$C_{\mathrm{n},0}$	0.0	[12]
$C_{\mathrm{S},0}$	0.0	[12]	$C_{\mathrm{m},\delta_{\mathrm{a}}}$	0.29	[12]
$C_{\mathrm{D},0}$	0.027	[12]	$C_{\mathrm{l},\delta_{\mathrm{e}}}$	0.81	[12]
$C_{\mathrm{L},\alpha}$	4.63	[12]	$C_{\mathrm{n},\delta_{\mathrm{r}}}$	0.04	[12]
$C_{\mathrm{D},\alpha}$	0.097	[12]	$C_{\mathrm{m},\alpha}$	-0.75	[12]
C_{D,α^2}	1.27	[12]	$C_{\mathrm{l},\beta}$	-0.058	[12]
$C_{\mathrm{S},\beta}$	-0.217	[12]	$C_{\mathrm{n},\beta}$	0.059	[12]
C_{D,β^2}	-0.162	[12]	$C_{\mathrm{l},\mathrm{p}}$	-0.55	[12]
$C_{\mathrm{S},\delta_{\mathrm{r}}}$	0.113	[12]	$C_{\mathrm{n},\mathrm{p}}$	-0.013	[12]
$C_{\mathrm{l},0}$	0.0	[12]	$C_{\mathrm{l},\mathrm{r}}$	0.06	[12]
$C_{\mathrm{m},0}$	0.0	[12]	$C_{\mathrm{n},\mathrm{r}}$	-0.045	[12]

The rotational degrees of freedom of the kth kite are described with a direct cosine matrix $\boldsymbol{R}_k = [\hat{\boldsymbol{e}}_{1,k}, \hat{\boldsymbol{e}}_{2,k}, \hat{\boldsymbol{e}}_{3,k}]$, whose unit vectors give the kite chord-wise, span-wise, and up axes, and an angular velocity vector $\boldsymbol{\omega}_k$. As a rotation matrix, $\boldsymbol{R}_k$ must be orthonormal:

$$P_{\mathrm{ut}} \left(\boldsymbol{R}_k^\top \boldsymbol{R}_k - \boldsymbol{I} \right) = \boldsymbol{0}, \qquad (1)$$

where the projection operator P_{ut} selects the six upper triangular elements [7]. The aileron-, elevator- and rudder-deflection, written as $\boldsymbol{\delta}_k = [\delta_{\mathrm{a},k}, \delta_{\mathrm{e},k}, \delta_{\mathrm{r},k}]^\top$, determine the aerodynamics of the kth kite. The deflection rates $\dot{\boldsymbol{\delta}}_k$ are used to control $\boldsymbol{\delta}_k$. A realistic kite geometry - wingspan b, mean aerodynamic chord c_{ref}, and planform area $S_{\mathrm{ref}} = bc_{\mathrm{ref}}$ - is chosen to correspond to the Ampyx AP2, a real power kite. These values, and other modelling parameters can be found in Table I.

Using this tree geometry, the dynamics of the MAWES can be formulated such that the behavior of the system can be studied at various wind velocities.

B. Dynamics

The MAWES mechanical power can be found when modelling the motion of the three degree-of-freedom tether nodes and the six degree-of-freedom kite nodes.

1) Translational dynamics: The translational MAWES dynamics can be described with Lagrangian dynamics using a set of generalized coordinates $\boldsymbol{q} = [\boldsymbol{q}_n^\top]^\top$.

The mass of a node is considered to be half of the mass of its connected tether segments. For kite nodes, the node mass additionally contains the mass of a kite m_{K}. Then, the node mass m_n can be found as:

$$m_n = m_{\mathrm{K}} \delta_{(n \in \mathcal{K})} + \frac{1}{2} \rho_{\mathrm{d}} \left(s_n l_n + \sum_c^{\mathcal{C}(n)} s_c l_c \right), \qquad (2)$$

where $\delta_{(n \in \mathcal{K})}$ is 1 for kite nodes and 0 otherwise, ρ_{d} is the tether density, and the tether diameter d_n gives the cross-sectional area $s_n = \pi d_n^2 / 4$.

Each node's potential energy V_n and kinetic energy T_n can be found, using g as the gravitational acceleration:

$$V_n = m_n g \, \boldsymbol{q}_n^\top \hat{\boldsymbol{z}}, \qquad T_n = \frac{1}{2} m_n \dot{\boldsymbol{q}}_n^\top \dot{\boldsymbol{q}}_n. \qquad (3)$$

The tether likely does not contribute much to the system inertia; however, the heavy generator drum which reels-in and -out may contribute. As such, the kinetic energy of the drum T_{W} is included in the Lagrangian dynamics, by assuming the drum is a solid cylinder of mass m_{W} which has a no-slip condition with the main tether:

$$T_{\mathrm{W}} = \frac{1}{4} m_{\mathrm{W}} \dot{l}_{\mathrm{T}}^2. \qquad (4)$$

The tethers constrain the distance between the nodes. With q_0 at the origin, the constraints for all $n \in \mathcal{N}$ read:

$$c_n = \frac{1}{2} \left((\boldsymbol{q}_n - \boldsymbol{q}_{n-1})^\top (\boldsymbol{q}_n - \boldsymbol{q}_{n-1}) - l_n^2 \right), \qquad (5)$$

and are concatenated into a vector $\boldsymbol{c}$. Similarly, the constraint multipliers λ_n can be concatenated into a vector $\boldsymbol{\lambda}$.

The Lagrangian of the MAWES is then given by

$$\mathcal{L} = \sum_n^{\mathcal{N}} T_n + T_{\mathrm{W}} - \sum_n^{\mathcal{N}} V_n - \boldsymbol{\lambda}^\top \boldsymbol{c}. \qquad (6)$$

Let the generalized force vector $\boldsymbol{F} = [\boldsymbol{F}_n^\top]^\top$ contain each node's external force $\boldsymbol{F}_n$. Then, the Lagrangian dynamics, after performing an index reduction on the holonomic constraints, are summarized by:

$$\frac{d}{dt} \frac{\partial \mathcal{L}}{\partial \dot{\boldsymbol{q}}} - \frac{\partial \mathcal{L}}{\partial \boldsymbol{q}} = \boldsymbol{F}, \qquad \ddot{\boldsymbol{c}} + 2\kappa \dot{\boldsymbol{c}} + \kappa^2 \boldsymbol{c} = 0. \qquad (7a)$$

Note that Baumgarte stabilization with parameter κ is applied to the constraint ($\ddot{c} = 0$) to preserve linear independence in a periodic context [7].

Using the tether tension $\boldsymbol{\tau}_n = \lambda_n l_n$, the tether stress σ_n must be within a safety factor f_{s} of the tether yield stress $\sigma_{\max}$. For $n \in \mathcal{N}$, this reads:

$$\frac{\boldsymbol{\tau}_n f_{\mathrm{s}}}{\sigma_{\max} s_{\max}} - \frac{s_n}{s_{\max}} \leq 0, \qquad (8)$$

where $s_{\max}$ is the cross-sectional area at the maximum tether diameter $d_{\max}$. For an undiscretized main tether, the main tether stress $\tau_{\mathrm{T}} = \tau_1$.

The dynamics of the remaining translational states read:

$$\frac{d[\boldsymbol{q}_n^\top, \boldsymbol{\delta}_k^\top, l_{\mathrm{T}}, \dot{l}_{\mathrm{T}}]^\top}{dt} - [\dot{\boldsymbol{q}}_n^\top, \dot{\boldsymbol{\delta}}_k^\top, \dot{l}_{\mathrm{T}}, \ddot{l}_{\mathrm{T}}]^\top = 0. \qquad (9)$$

2) Rotational dynamics: The tethers are assumed to hold the kites at their center of mass. Then, $\boldsymbol{\omega}_{\mathrm{x},k}$, the skew-symmetric matrix of $\boldsymbol{\omega}_k$, the kite moment of inertia $\boldsymbol{J}$, and the external moment $\boldsymbol{M}_k$ about the body-fixed axes, give the rotational dynamics of the kth kite as:

$$\frac{d\boldsymbol{R}_k}{dt} - \boldsymbol{R}_k \boldsymbol{\omega}_{\mathrm{x},k} = 0, \qquad (10a)$$

$$\boldsymbol{J} \frac{d\boldsymbol{\omega}_k}{dt} + \boldsymbol{\omega}_k \times (\boldsymbol{J}\boldsymbol{\omega}_k) - \boldsymbol{M}_k = 0. \qquad (10b)$$

TABLE II: Variable bounds, $\hat{e}_i \in \{\hat{x}, \hat{y}, \hat{z}\}$, sf $\in \{a, e, r\}$

ν	$\nu_{\min}$	$\nu_{\max}$	units	ν	$\nu_{\min}$	$\nu_{\max}$	units
$q_n^\top \hat{z}$	10	$5 \cdot 10^3$	m	l_{T}	0	10^4	m
$\ddot{q}_n^\top \hat{e}_i$	$-12g$	$12g$	m/s^2	$\dot{l}_{\mathrm{T}}$	$-\infty$	$5u_{\mathrm{ref}}$	m/s
$\delta_{\mathrm{a},k}$	-0.35	0.35	rad	$\ddot{l}_{\mathrm{T}}$	-15	15	m/s^2
$\delta_{\mathrm{e},k}$	-0.52	0.52	rad/s	l_{S}	b	$100b$	m
$\delta_{\mathrm{r},k}$	-0.52	0.52	rad/s	d_n	10^{-3}	10^{-1}	m
λ_n	0	10^4	N/m	t_{f}	0	500	s
$\dot{\delta}_{\mathrm{sf}}$	-2	2	rad/s^2	α	-7.4	21.8	deg
β	-15	15	deg				

3) Energy dynamics: The energy produced by the MAWES is the integrated instantaneous mechanical power:

$$\dot{E} = P = \tau_{\mathrm{T}} \dot{l}_{\mathrm{T}}, \tag{11}$$

where P is the instantaneous power produced, with $\overline{P} = E(t_{\mathrm{f}})/t_{\mathrm{f}}$ the average power over the pumping cycle period t_{f}. The energy starts the pumping cycle at zero:

$$E(t_0) = 0. \tag{12}$$

A number of bounds are applied in order to preclude non-physical solutions, such as subterranean flight, and compressive tether forces. For the variables named in Table II, these bounds read as:

$$\nu_{\min} \leq \nu \leq \nu_{\max}. \tag{13}$$

With the dynamic framework in place, the MAWES model now needs to find F_n and M_k using an aerodynamic model.

C. Aerodynamic model

The aerodynamics of the tether and kites are determined by their motion within the modelled atmosphere, including simplified wake modelling.

1) Atmosphere: For simplicity, the atmosphere is approximated as a steady boundary layer, despite not well representing altitudes above 500m or instantaneity. This model, as well as parameters appropriate to the AWE context, are given in [11], with international standard atmosphere relations for temperature $T(z)$, density $\rho(z)$, a log-wind profile for the free-stream velocity $u_\infty(z)$, and dynamic pressure $q_\infty(z)$:

$$u_\infty(z) = u_{\mathrm{ref}} \frac{\log \frac{z}{z_0}}{\log \frac{z_{\mathrm{ref}}}{z_0}} \hat{x}, \qquad q_\infty(z) = \frac{1}{2}\rho(z) u_\infty^\top u_\infty, \tag{14}$$

where the reference wind velocity $u_{\mathrm{ref}} = u_{\mathrm{ref}}\hat{x}$ is measured at altitude z_{ref}, and z_0 is the roughness length.

2) Tether aerodynamics: The drag force $F_{\mathrm{S},n}$ on the nth segment of tether is determined by approximating the tether segment as a non-rotating cylinder, with an average velocity and altitude $z_n = (q_n + q_{P(n)})^\top \hat{z}/2$ from the segment endpoints:

$$F_{\mathrm{S},n} = \frac{C_{\mathrm{T}}}{2} \rho(z_n) \|u_{\mathrm{a},n}\|_2 \, d_n l_n u_{\mathrm{a},n}, \tag{15}$$

using the tether drag coefficient C_{T} and $u_{\mathrm{a},n}$ is the apparent velocity of the midpoint of the tether:

$$u_{\mathrm{a},n} = u_\infty(z_n) - \frac{1}{2}\left(\dot{q}_n + \dot{q}_{P(n)}\right). \tag{16}$$

The tether drag on a given segment of tether is shared equally between the segment's two endpoints. The decision

to use this first order approximation was made to limit model complexity. One caveat is that the approximation underestimates the effective moment on the kites from secondary tether drag.

The nth node experiences a tether drag $F_{\mathrm{N},n}$ found as:

$$F_{\mathrm{N},n} = \frac{1}{2}\left(F_{\mathrm{S},n} + \sum_c^{\mathcal{C}(n)} F_{\mathrm{S},c}\right). \tag{17}$$

For nodes that do not have kites ($n \notin \mathcal{K}$), the external force is purely the tether drag force: $F_n = F_{\mathrm{N},n}$.

3) Axial induction approximation: The wind velocity at the kite is different from the free-stream described in (14) due to induction, the wind field's reaction to the aerodynamic force exerted by the kite. The actuator disk (AD) method gives a first-order induction model. The AD determines the induced velocity at the kite by requiring the flow to decrease its momentum to compensate for the aerodynamic force on the kite along the axis of rotation.

The AD approximation assumes that the kite orbit axis of rotation, the main tether, and the free-stream wind direction are aligned; that wake expansion and rotation is negligible; and that the flow is potential, in equilibrium, and uniform within a stream-tube cross-section containing the kites. Following the derivation applied for conventional wind turbines [13], the AD approximation reads:

$$4 q_\infty \left(q_{\mathrm{c}}^\top \hat{z}\right) A \, a(1-a) - \hat{e}_{\mathrm{T}}^\top \left(\sum_k^{\mathcal{K}} F_k\right) = 0, \tag{18a}$$

$$0 \leq a \leq 0.4, \tag{18b}$$

where $q_{\mathrm{c}} = \sum_k^K q_k/|\mathcal{K}|$ is the arithmetic center of the kites.

Here, the annulus area A is approximated as an average of the annuli approximated per kite. Each kite's annulus is defined by an outer radius from the outer wing-tip to q_{c}, and an inner radius to the inner wing-tip. This approximation was chosen for its simplicity, as it can be computed in both the reel-in and reel-out phases.

$$A = \sum_k^{\mathcal{K}} \frac{4\pi}{|\mathcal{K}|} \left(\frac{1}{2}b\hat{e}_{2,k}\right)^\top (q_k - q_{\mathrm{c}}). \tag{19}$$

4) Kite aerodynamics: Given the wind velocity defined previously, aerodynamic stability derivatives describe the kite's aerodynamics [8].

With apparent velocity $u_{\mathrm{a},k} = u_\infty(q_k^\top \hat{z})(1-a) - \dot{q}_k$, the kth kite's orientation with respect to the flow is given by the angle-of-attack α_k and the side-slip angle β_k:

$$\alpha_k = \frac{u_{\mathrm{a},k}^\top \hat{e}_{3,k}}{u_{\mathrm{a},k}^\top \hat{e}_{1,k}}, \qquad \beta_k = \frac{u_{\mathrm{a},k}^\top \hat{e}_{2,k}}{u_{\mathrm{a},k}^\top \hat{e}_{1,k}}, \tag{20}$$

where the flow remains attached by requiring that:

$$\alpha_{\min} \leq \alpha_k \leq \alpha_{\max}, \qquad \beta_{\min} \leq \beta_k \leq \beta_{\max}. \tag{21}$$

The aerodynamic force and moment coefficients of the kth kite - drag $C_{\mathrm{D},k}$, side $C_{\mathrm{S},k}$, lift $C_{\mathrm{L},k}$, roll $C_{l,k}$, pitch $C_{\mathrm{m},k}$, and yaw $C_{\mathrm{n},k}$ - can be found

with the standard linearizations about α_k, β_k, $\boldsymbol{\delta}_k$, and $\mathrm{diag}([b, c_{\mathrm{ref}}, b])\ \boldsymbol{\omega}_k/(2\,||\boldsymbol{u}_{\mathrm{a},k}||_2)$.

Then, the aerodynamic force $\boldsymbol{F}_{\mathrm{K},k}$ and moment $\boldsymbol{M}_k$ on the kth kite can be found, using the dynamic pressure $q_k = \frac{1}{2}\rho(\boldsymbol{q}_k^\top \hat{\boldsymbol{z}})\ ||\boldsymbol{u}_{\mathrm{a},k}||_2^2$, and the abbreviations $\mathrm{c}_\alpha = \cos\alpha_k$, $\mathrm{s}_\alpha = \sin\alpha_k$, $\mathrm{c}_\beta = \cos\beta_k$, and $\mathrm{s}_\beta = \sin\beta_k$:

$$\boldsymbol{F}_{\mathrm{K},k} = q_k S_{\mathrm{ref}} \boldsymbol{R}_k \begin{pmatrix} \mathrm{c}_\alpha\mathrm{c}_\beta & -\mathrm{c}_\alpha\mathrm{s}_\beta & -\mathrm{s}_\alpha \\ \mathrm{s}_\beta & \mathrm{c}_\beta & 0 \\ \mathrm{c}_\beta\mathrm{s}_\alpha & -\mathrm{s}_\alpha\mathrm{s}_\beta & \mathrm{c}_\alpha \end{pmatrix} \begin{pmatrix} C_{\mathrm{D},k} \\ C_{\mathrm{S},k} \\ C_{\mathrm{L},k} \end{pmatrix}, \quad (22\mathrm{a})$$

$$\boldsymbol{M}_k = q_k S_{\mathrm{ref}} \begin{pmatrix} b & 0 & 0 \\ 0 & c_{\mathrm{ref}} & 0 \\ 0 & 0 & b \end{pmatrix} \begin{pmatrix} C_{\mathrm{l},k} \\ C_{\mathrm{m},k} \\ C_{\mathrm{n},k} \end{pmatrix}. \quad (22\mathrm{b})$$

For kite nodes $k \in \mathcal{K}$, the external force sums the tether force (17) and the kite force: $\boldsymbol{F}_k = \boldsymbol{F}_{\mathrm{N},k} + \boldsymbol{F}_{\mathrm{K},k}$.

To prevent the solution from leaving the incompressible flow regime where the stability derivative linearizations are valid, the MAWES Mach numbers - calculated for dry air using the heat capacity ratio γ and the gas constant R - are restricted:

$$\frac{||\boldsymbol{u}_{\mathrm{a},k}||_2}{\sqrt{\gamma\,R\,T(\boldsymbol{q}_k^\top \hat{\boldsymbol{z}})}} - 0.3 \le 0. \quad (23)$$

D. Periodicity

Assuming periodic MAWES trajectories in steady wind conditions requires that the initial and final states are equivalent:

$$\xi(t_{\mathrm{f}}) - \xi(t_0) = 0, \quad (24)$$

where $\xi \in [\boldsymbol{q}_n^\top, \dot{\boldsymbol{q}}_n^\top, \boldsymbol{\omega}_k^\top, \boldsymbol{\delta}_k^\top, l_{\mathrm{T}}, \dot{l}_{\mathrm{T}}]^\top$. To prevent a linear dependence with the rotation matrix orthonormality (1), the projection method [7] is employed to enforce the periodicity of $\boldsymbol{R}_k$ as

$$P_{\mathrm{lt}}\left(\boldsymbol{R}_k(t_0)^\top \boldsymbol{R}_k(t_{\mathrm{f}}) - I\right) = \boldsymbol{0}, \quad (25)$$

where the projection operator P_{lt} selects the three lower triangular elements.

Using the MAWES model described to this point, it remains to formulate an OCP capable of optimizing MAWES trajectories at different wind speeds.

III. OCP TO MAXIMIZE AVERAGE POWER

A power-maximization periodic optimal control problem is formulated using the previously described model:

$$\underset{\boldsymbol{x}}{\text{minimize}} \quad -\overline{P} + \boldsymbol{x}^\top \boldsymbol{W} \boldsymbol{x} \quad (26\mathrm{a})$$

$$\text{subject to} \quad (1), (7)-(13), (18), (21), (23)-(25) \quad (26\mathrm{b})$$

The decision variables $\boldsymbol{x} = [\boldsymbol{w}^\top, \boldsymbol{\theta}^\top]^\top$ include time-varying states, algebraic variables, and controls $\boldsymbol{w} = [\boldsymbol{q}_n^\top, \dot{\boldsymbol{q}}_n^\top, \mathrm{vec}\,(\boldsymbol{R}_k)^\top, \boldsymbol{\omega}_k^\top, \boldsymbol{\delta}_k^\top, l_{\mathrm{T}}, \dot{l}_{\mathrm{T}}, E, a, \lambda_n, \dot{\boldsymbol{\delta}}_k^\top, \ddot{l}_{\mathrm{T}}]^\top$; and parameters $\boldsymbol{\theta} = [d_{\mathrm{T}}, d_{\mathrm{S}}, l_{\mathrm{S}}, t_{\mathrm{f}}]^\top$. These variables are regularized with a small diagonal weighting matrix $\boldsymbol{W}$.

Direct collocation is employed with Radau polynomials of degree 4 in 20 collocation intervals. A homotopy strategy similar to [14] is used to generate a feasible initial guess for the problem, after which (26) can typically be solved within

one minute. The NLP is formulated in the algorithmic differentiation frame-work CasADi [15] in Python, and solved by the interior point NLP solver IPOPT [16], using the linear solver MA57 [17].

IV. RESULTS

First, (26) is solved at a typical reference wind speed [11] of $u_{\mathrm{ref}}^* = 5$ m/s, to find reasonable values for the geometric parameters $\boldsymbol{\theta}$: secondary tether-length $l_{\mathrm{S}} = 72$ m, and diameter $d_{\mathrm{S}} = 7.0$ mm, and main tether diameter $d_{\mathrm{T}} = 8.7$ mm. These values are frozen by modifying the bounds of (13), while the period t_{f} remains free. Then, (26) is solved over a range of reference wind speeds $\upsilon = u_{\mathrm{ref}}/u_{\mathrm{ref}}^* \in [0.2, 3]$, a region limited by the ability of the solver to find a feasible solution.

A. Operational regions for MAWES

At different wind velocities, three distinct regions of MAWES behavior are found. The average power $\overline{P}(\upsilon)$ and the average power harvesting factor $\overline{\zeta}(\upsilon)$ are shown in Figure 2, where $\overline{\zeta}$ is the time average of the instantaneous power harvesting factor $\zeta = P/\left(q_\infty(\boldsymbol{q}_1^\top \hat{\boldsymbol{z}})\ ||\boldsymbol{u}_\infty(\boldsymbol{q}_1^\top \hat{\boldsymbol{z}})||_2\ |\mathcal{K}|\,S_{\mathrm{ref}}\right)$ [1].

In Region I, the wind speed is not sufficient for the MAWES to harvest energy, and the system consumes energy to remain aloft. In Region II, the system is effectively 'over-designed' for the wind conditions, such that the power harvesting factor increases with the wind speed. In Region III, the system limits its energy extraction, due to active tether stress constraints. For the studied MAWES, the boundary between Regions I and II lays at $\upsilon_{\mathrm{I}} = 0.37$; between Regions II and III, at the 'design' reference wind speed $\upsilon_{\mathrm{III}} = 1$. MAWES behavior and preliminary aerodynamic modelling applicability to Regions II, III, and I are described, respectively, in subsections IV-B, IV-C, and IV-D.
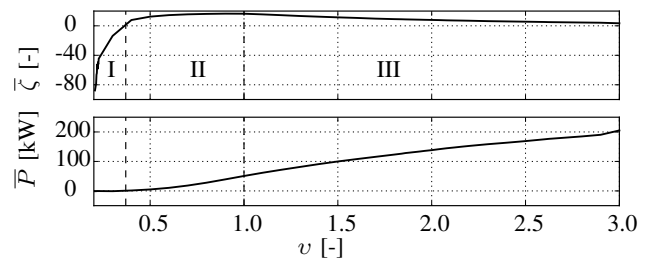

Fig. 2: Average power harvesting factor $\overline{\zeta}$ and average power $\overline{P}$ vs. reference velocity ratio υ, for Regions I, II, and III.

B. Region II and the design case

When $u_{\mathrm{ref}}^* = 5$ m/s and $\upsilon = 1$, the solution predicts an average power of $\overline{P} = 51.7$ kW with an average power harvesting factor $\overline{\zeta} = 16.5$. This estimate of power production from a two-kite MAWES is approximately 25 times larger than the 2 kW predicted for a single-kite AP2 in the same wind conditions [18]. This increase appears very large - even considering the doubling in planform area - as drag-mode systems [3] have been predicted to produce
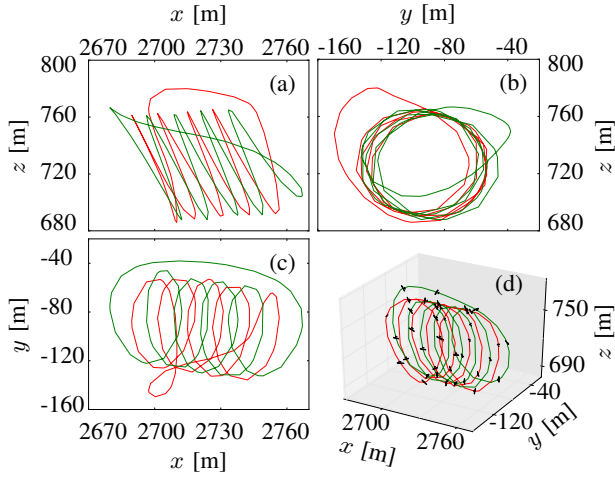
Fig. 3: Trajectory at design-case, $\upsilon = 1$, $u^*_{\text{ref}} = 5$ m/s, in (a) side-, (b) downstream-, (c) top-, (d) isometric-view.
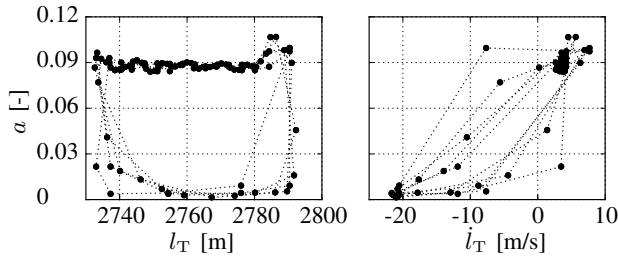

Fig. 4: Induction factor a vs. (left) main tether length l_{T}, and (right) reel-out velocity $\dot{l}_{\text{T}}$, for design case with $\upsilon = 1$.

Fig. 5: Trajectory in Region III, $\upsilon = 2.8$, in (a) side-, (b) downstream-, (c) top-, (d) isometric-view.
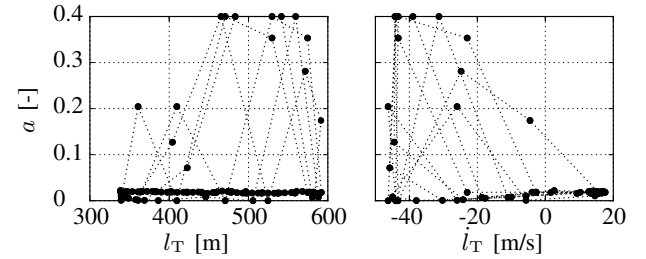
Fig. 6: Induction factor a vs. (left) main tether length l_{T}, and (right) reel-out velocity $\dot{l}_{\text{T}}$, in Region III with $\upsilon = 2.8$.

six times more power in a two-kite MAWES configuration compared to a single-kite system of equal total planform area. This large value may be due to the underestimation of tether drag mentioned previously.

The solution cannot be guaranteed to be a global solution, but it appears to be meaningful. As expected, the trajectory (Figure 3) has a helical reel-out phase, with a swooping reel-in that decreases the component of force along the main tether. At $\upsilon = 1$, the average reel-out factor during the reel-out phase $\overline{f}_{\text{out}} = 0.39$ falls close to the Loyd single-kite optimum of one-third, using the instantaneous reel-out factor $f = \dot{l}_{\text{T}} / \left\| \boldsymbol{u}_\infty (\boldsymbol{q}_1^\top \hat{\boldsymbol{z}}) \right\|_2$.

The induction factors, describing the energy extracted from the wind, shown in Figure 4, follow a cycle of very small values during reel-in, and moderate values - limited by the tether stress constraint - during the reel-out. Considering the light loading of the AD annulus shown by the induction factors less than 1/3, small elevation angles between 10-15°, and the orbit about the free-stream wind axis as in Figure 3, no indications were found that AD-type methods are invalid in Region II. However, the average Region II Reynolds number of $1.8 \cdot 10^6$ may recommend models valid over flow transition.

C. Region III behavior

The geometric parameters were sized with active tether stress constraints when $\upsilon = 1$. As the wind speed increases,
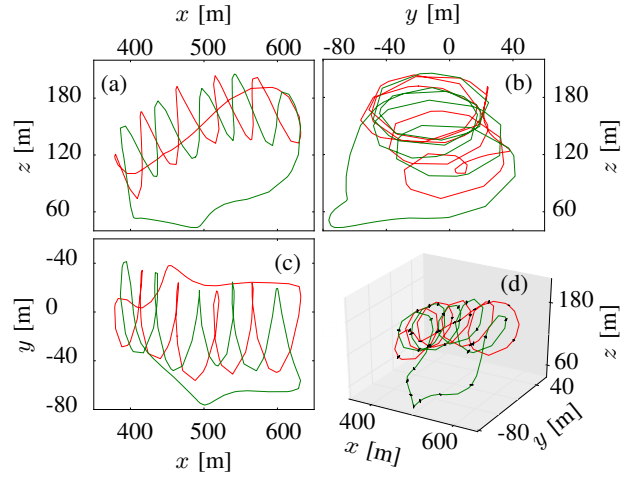
the MAWES must become less efficient at harvesting energy or these stress constraints will be violated. In response, the flight altitude decreases (see Figure 5) and the average reel-out factor increases, reaching the value $\overline{f}_{\text{out}} = 0.68$ at $\upsilon = 2.8$. Additionally, the average elevation angle increases - to 12° in Region II and 15° in Region III - increasing the cosine losses due to tether and wind misalignment. Further, the helical trajectory tightens as induction effects become less relevant. To extract less energy from the flow, the induction factors drop (Figure 6) until they are very small except during the strongest reel-in. Further study is needed to assess whether such jumps are consistent with the AD assumption of equilibrated flow.

D. Region I behavior

In Region I, the optimizer prefers trajectories that stay aloft at a minimum power cost. These 'holding patterns' appear to orbit primarily about the $\hat{\boldsymbol{z}}$ axis, as seen in Figure 7, to allow the lift force to better counteract gravity. Such a vertical orbit is fundamentally inconsistent with the AD assumptions. As such, wake modelling methods that are more flexible than the - very inexpensive - AD are required for the study of landing in Region I, leading to larger and more nonlinear OCPs.

V. CONCLUSION

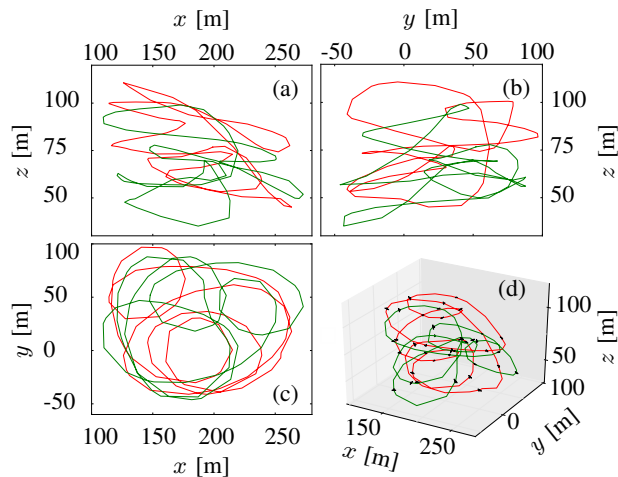In this paper, two-kite pumping-cycle MAWES behavior has been considered for different wind velocities. Analogous

Fig. 7: Trajectory in Region I, $\upsilon = 0.2$, in (a) side-, (b) downstream-, (c) top-, (d) isometric-view.

to wind turbines, there are three distinct operational regions for MAWES: Region I, where power is consumed to stay aloft, Region II, where the power harvesting factor grows until the design wind speed, and Region III where the system intentionally limits power extraction to respect its physical limitations. Results also indicate that Region I modelling requires a more flexible wake modelling method than AD, though this will likely lead to an increase in OCP size, non-linearity and expense. Further assessment of wake-modelling strategies within MAWES OCPs is in progress.

REFERENCES

[1] M. Diehl, "Airborne Wind Energy: Basic Concepts and Physical Foundations," in *Airborne Wind Energy*, U. Ahrens, M. Diehl, and R. Schmehl, Eds., Heidelberg, Germany: Springer, 2014, ch. 1, pp. 3–22.

[2] B. Houska and M. Diehl, "Optimal control for power generating kites," in *Proc European Control Conference*, 2007, pp. 1–14.

[3] M. Zanon, S. Gros, J. Andersson, and M. Diehl, "Airborne Wind Energy Based on Dual Airfoils," *IEEE Transactions on Control Systems Technology*, vol. 21, no. 4, pp. 1215–1222, 2013.

[4] M. Zanon, G. Horn, S. Gros, and M. Diehl, "Control of Dual-Airfoil Airborne Wind Energy Systems Based on Nonlinear MPC and MHE," in *2014 European Control Conference (ECC)*, Strasbourg, France, 2014.

[5] M. Zanon, S. Gros, J. Meyers, and M. Diehl, "Airborne Wind Energy: Airfoil-Airmass Interaction," in *Proceedings of the 19th World Congress The International Federation of Automatic Control*, Cape Town, South Africa, 2014.

[6] R. Leuthold, S. Gros, and M. Diehl, "Induction in Optimal Control of Multiple-Kite Airborne Wind Energy Systems," in *Proceedings of the 20th World Congress The International Federation of Automatic Control*, Toulouse, France, 2017.

[7] S. Gros and M. Zanon, "Numerical Optimal Control with Periodicity Constraints in the Presence of Invariants," '*IEEE Transactions on Automatic Control*', under revision.

[8] G. Licitra, P. Williams, J. Gillis, S. Ghandchi, S. Sieberling, R. Ruiterkamp, and M. Diehl, "Aerodynamic Parameter Identification for an Airborne Wind Energy Pumping System," in *Proceedings of the 20th World Congress The International Federation of Automatic Control*, Toulouse, France, 2017.

[9] R. Bosman, V. Reid, M. Vlasblom, and P. Smeets, "Airborne wind energy tethers with high-modulus polyethylene fibers," in *Airborne Wind Energy*, U. Ahrens, M. Diehl, and R. Schmehl, Eds., Heidelberg, Germany: Springer, 2014, ch. 33, pp. 563–586.

[10] R. von Mises, *Theory of flight*, 2nd ed. New York, New York, USA: Dover, 1959.

[11] C. L. Archer, "An Introduction to meteorology for airborne wind energy," in *Airborne Wind Energy*, U. Ahrens, M. Diehl, and R. Schmehl, Eds., Heidelberg, Germany: Springer, 2014, ch. 6, pp. 81–94.

[12] G. Licitra, "Numerical optimal trajectory for system in pumping mode described by differential algebraic equation (focus on AP2)," Ampyx Power B.V., Den Haag, Netherlands, Tech. Rep., 2014.

[13] E. Branlard, *Wind turbine aerodynamics and vorticity-based methods : fundamentals and recent applications*. Roskilde, Denmark: Springer, 2017.

[14] S. Gros, M. Zanon, and M. Diehl, "A relaxation strategy for the optimization of Airborne Wind Energy systems," in *Proceedings of the European Control Conference (ECC)*, Zurich, Switzerland, 2013, pp. 1011–1016.

[15] J. Andersson, J. Åkesson, and M. Diehl, "CasADi: A Symbolic package for automatic differentiation and optimal control," in *Recent Advances in Algorithmic Differentiation*, S. Forth, P. Hovland, E. Phipps, J. Utke, and A. Walther, Eds., Berlin, Germany: Springer Berlin Heidelberg, 2012, pp. 297–307.

[16] A. Wächter and L. Biegler, "On the implementation of a primal-dual interior point filter line search algorithm for large-scale nonlinear programming," *Mathematical Programming*, vol. 106, no. 1, pp. 25–57, 2006.

[17] *HSL. A collection of Fortran codes for large scale scientific computation.* [Online]. Available: http://www.hsl.rl.ac.uk/.

[18] G. Licitra, J. Koenemann, G. Horn, P. Williams, R. Ruiterkamp, and M. Diehl, "Viability assessment of a rigid wing airborne wind energy pumping system," in *2017 21st International Conference on Process Control (PC)*, Jun. 2017, pp. 452–458.